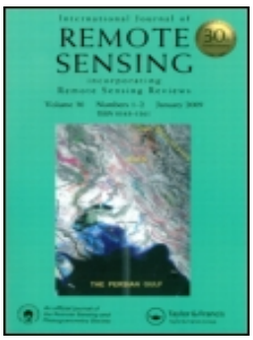

International Journal of Remote Sensing

ISSN: 0143-1161 (Print) 1366-5901 (Online) Journal homepage: http://www.tandfonline.com/loi/tres20

A KPCA texture feature model for efficient segmentation of RADARSAT-2 SAR sea ice imagery

Linlin Xu, Jonathan Li, Alexander Wong & Cheng Wang

To cite this article: Linlin Xu, Jonathan Li, Alexander Wong & Cheng Wang (2014) A KPCA texture feature model for efficient segmentation of RADARSAT-2 SAR sea ice imagery, International Journal of Remote Sensing, 35:13, 5053-5072, DOI: 10.1080/01431161.2014.933279

To link to this article: http://dx.doi.org/10.1080/01431161.2014.933279

International Journal of Remote Sensing, 2014
Vol. 35, No. 13, 5053–5072, http://dx.doi.org/10.1080/01431161.2014.933279

A KPCA texture feature model for efficient segmentation of RADARSAT-2 SAR sea ice imagery

Linlin Xu[a], Jonathan Li[a,b]*, Alexander Wong[c], and Cheng Wang[b]

[a]*Department of Geography and Environmental Management, University of Waterloo, Waterloo, Ontario, Canada N2L 3G1;* [b]*Key Laboratory for Underwater Acoustic Communication and Marine Information Technology, Xiamen University, Xiamen, Fujian 361005, China;* [c]*Department of System Design Engineering, University of Waterloo, Waterloo, Ontario, Canada N2L 3G1*

(*Received 14 July 2013; accepted 21 March 2014*)

Sea ice information obtained from synthetic aperture radar (SAR) images is crucial for ensuring safe marine navigation and supporting climate change studies in polar regions. We propose a kernel principal component analysis (KPCA) local texture feature model for efficient sea ice segmentation. The proposed KPCA texture feature model is significant for several reasons. First, it takes into account the multiplicative nature of SAR speckle noise. The resulting KPCA features therefore assume independent and identically distributed (i.i.d.) Gaussian-like noise, which satisfies the assumptions inherent in classical statistical models such as the *k*-means algorithm. Second, the KPCA features are compact and statistically independent and therefore capable of reducing data redundancy. Third, the KPCA texture features are discriminative. Finally, the extraction of KPCA features requires less computation. Based on the KPCA model, a segmentation scheme is implemented in four steps. First, local patch-based texture descriptors are extracted from the image. Second, KPCA is performed on the patch-based texture descriptors to obtain compact and discriminative texture features with Gaussian-like noise characteristics. Third, the *k*-means algorithm is performed on extracted KPCA features to segment the image. Finally, a neighbourhood-based majority voting scheme is employed to determine the final label of each pixel. We compared the proposed method with several other popular sea ice segmentation approaches. The results demonstrated that our method is robust to speckle noise level, is accurate and fast and may thus better support the operational segmentation of sea ice in SAR imagery.

1. Introduction

Space-borne synthetic aperture radar (SAR), due to its ability to cover large inaccessible areas without being affected by weather conditions or sunlight illumination, provides a powerful tool for sea ice monitoring, which is crucial for ensuring safe marine navigation and supporting climate change studies in polar regions. The RADARSAT-1 and -2 satellites have been the primary source of data for sea ice monitoring. At the Canadian Ice Service (CIS), the operational interpretation of SAR sea ice images relies on human operators to manually process a great number of image scenes annually. The sea ice charts, as the final product, label each identified region with an 'egg code' (see Figure 3), which indicates sea ice information (e.g. the type, concentration, stage of development, and floe size). This visual interpretation of SAR sea ice images, although capable of incorporating human knowledge and experiences, is very demanding because of the vast number of daily sea ice

*Corresponding author. Email: junli@uwaterloo.ca

observations. Hence, the designing of automatic programs that are capable of accurately and time-efficiently discerning the types and extent of sea ice is urgently needed. Although multichannel polarimetric SAR sensors have been used for sea ice segmentation (Rivas and Stoffelen 2011; Swan and Long 2012), they have not been used for operational sea ice monitoring. Single polarization SAR images collected by RADARSAT-1 and -2 ScanSAR beam mode are in the operational line of sea ice monitoring at CIS (Ochilov and Clausi 2012). We therefore focus on single polarization SAR images.

Although different sea ice types assume different grey tone values in SAR images, the complex sea ice physics and ever-changing ocean environment, as well as the numerous sensor parameters, cause large within-class grey tone variation. This significant within-class variation imposes a fundamental challenge for the automatic techniques for sea ice image segmentation. Current algorithms for SAR sea ice image segmentation can be categorized as pixel-based and texture-based. The former clusters pixels based on grey tone values, e.g. local thresholding (Havercamp, Soh, and Tsatsoulis 1993), Gamma (Samadani 1995), and Gaussian (Karvonen 2004) mixture models and *k*-means clustering (Redmund, Long, and Drinkwater 1998). Because of the sensitivity of single pixels to speckle noise, these methods always produce many artefacts. The suppression of speckle noise using denoising methods (Lee 1980; Frost et al. 1982; Kuan et al. 1985), however, will introduce new problems, such as blurring of the ice boundaries, which serve as important information to delineate sea ice.

As opposed to using single pixels, the texture-based approaches use texture features for segmentation, which are linear or nonlinear functions of neighbouring pixels, e.g. variation (Burns, Kasischke, and Nuesch 1982; Heolbaek-Hansen et al. 1989), grey-level co-occurrence matrix (GLCM) (Haralick, Shanmugam, and Dinstein 1973; Shuchman et al. 1989; Baraldi and Parmiggiani 1995; Barber and Ledrew 1991; Soh and Tsatsoulis 1999; Clausi 2002), Markov random fields (MRF) (Deng and Clausi 2005) and Gabor filter (Clausi 2001). Compared with the pixel-based approach, these methods are less sensitive to within-class variation. However, because of the vast number of individual texture features and their different characteristics, it is difficult to select the best group of features for the current task at hand. Moreover, most texture-based approaches are computationally intensive, thus are not suitable for operational use. This article therefore aims to explore a sea ice segmentation technique that is both efficient and accurate.

This article presents a fast and accurate approach for efficient segmentation of SAR sea ice images based on a kernel principal component analysis (KPCA) local texture feature model. A SAR image patch stack is formed by extracting an image patch for each pixel in the image. KPCA features are then extracted from the patch stack to feed into the *k*-means clustering algorithm for SAR sea ice image segmentation. The proposed KPCA texture feature model is significant for several reasons. First, it takes into consideration the multiplicative nature of the SAR speckle noise. The resulting KPCA features assume independent and identically distributed (i.i.d.) Gaussian-like noise, which is compatible with the assumptions of most popular statistical models such as the *k*-means method. Second, the KPCA features are compact and statistically independent and thus capable of reducing the data redundancy. Third, the KPCA local texture features are discriminative. KPCA works in a totally data-driven manner and seeks to reveal the 'best' texture patterns that produce the largest variation across different classes. Finally, the extraction of KPCA features requires less computation than other texture features such as GLCM. Moreover, KPCA features are compatible with the *k*-means algorithm, which is also very fast. Given these theoretical advantages, the segmentation scheme based on KPCA is both effective and time-efficient, thus may better support the operational segmentation of sea ice.

2. Theoretical background and motivation

In this article, we denote the discrete lattice spanned by a SAR sea ice image by N and a site in the lattice by $t \in N$. We represent the image patch centred at site t by $\boldsymbol{y}_t$, a p-dimensional random vector that takes on different greyscale values, and the label of site t by l_t, a random variable that takes on one of the classes in the set $\{1, \ldots, K\}$. Then the SAR sea ice image can be denoted as $\mathbf{Y} = \{\boldsymbol{y}_t | t \in N\}$ and the labels of this image as $\boldsymbol{l} = \{l_t | t \in N\}$. For SAR sea ice segmentation, we are trying to infer $\boldsymbol{l}$ based on $\mathbf{Y}$, which can be formulated as a maximum likelihood problem based on a Gaussian mixture model (GMM). We express the image patch in class $l_t = i$ ($i = 1 \ \ldots \ K$) as:

$$\boldsymbol{y}_t^i = \boldsymbol{\mu}^i + \boldsymbol{n}^i, \tag{1}$$

$$P\left(\boldsymbol{n}_t^i\right) = (2\pi)^{-p/2} |\boldsymbol{\Lambda}_i|^{-1/2} \exp\left\{-1/2 \boldsymbol{n}_t^{i\mathrm{T}} \boldsymbol{\Lambda}_i^{-1} \boldsymbol{n}_t^i\right\}, \tag{2}$$

$$P\left(\boldsymbol{y}_t^i\right) = (2\pi)^{-p/2} |\boldsymbol{\Lambda}_i|^{-1/2} \exp\left\{-1/2 \left(\boldsymbol{y}_t^i - \boldsymbol{\mu}^i\right)^{\mathrm{T}} \boldsymbol{\Lambda}_i^{-1} \left(\boldsymbol{y}_t^i - \boldsymbol{\mu}^i\right)\right\}, \tag{3}$$

where P stands for probability, $\boldsymbol{\mu}^i$ and $\boldsymbol{n}^i$ are, respectively, the mean value and noise for class i, and $\boldsymbol{\Lambda}_i$ is the covariance matrix of $\boldsymbol{n}^i$. Assuming that image patches are independent, the optimal $\boldsymbol{l}$ can be estimated by maximizing the log-likelihood of $\mathbf{Y}$.

$$\hat{\boldsymbol{l}} = \arg\max_{l} \left\{ \sum_{t=1}^{N} \ln \left[\sum_{i=1}^{K} P(l_t = i) P\left(\boldsymbol{y}_t^i\right) \right] \right\}. \tag{4}$$

Since image patches $\boldsymbol{y}_t$ characterize the spatial relationship of local pixels, using image patches instead of individual pixels would allow better representation of texture patterns and thus be more capable of resisting the influence of speckle noise. However, the drawbacks of using $\boldsymbol{y}_t$ lie in the fact that $\boldsymbol{y}_t$ assumes a high level of noise, high dimensionality, and that $\boldsymbol{y}_t$ itself may not reveal the most discriminative texture patterns. Therefore, one essential issue for sea ice segmentation is to explore the most compact and discriminative texture features as model input. Many texture features as linear or nonlinear transformations of $\boldsymbol{y}_t$ have been used instead of $\boldsymbol{y}_t$, as in the GLCM (Haralick, Shanmugam, and Dinstein 1973; Clausi 2002) and Gabor filter (Clausi 2001) methods, for example. However, because of the huge degree of variability in these texture features and their varying characteristics, it is difficult to select the best group of features for the current task at hand. Moreover, it is difficult to predict the statistical distribution of texture features. In Section 3.2, we present a KPCA model to extract compact and discriminative texture features with Gaussian-like noise characteristics. We illustrate that the proposed KPCA local texture features assume some meaningful characteristics that benefit sea ice segmentation.

Another essential issue in probabilistic sea ice segmentation is to ensure that the distribution of $\boldsymbol{n}^i$ satisfies the assumptions of the clustering model employed. In this article, we use the k-means algorithm as a special case of Equation (4) for sea ice segmentation. While the k-means algorithm is simple and fast, it imposes a strict assumption on $\boldsymbol{n}^i$. Nevertheless, in Section 3.3, we prove that the KPCA features well satisfy the k-means assumption about noise distribution. Therefore, theoretically speaking, the performance of the k-means algorithm can be optimized.

3. Kernel principal component analysis texture model

In this section, we first briefly introduce the KPCA approach. Then we explain the extraction of texture features based on the KPCA approach as well as the interpretation of the extracted features. Finally, we explore the compatibility of KPCA texture features with the *k*-means algorithm.

3.1. Kernel principal component analysis

Similar to classic principal component analysis (PCA), the KPCA approach intends to obtain a series of orthogonal directions that explain most of the data variance. However, KPCA works in nonlinear feature space rather than the original space (Schölkopf, Smola, and Müller 1998). As such, the KPCA is supposed to be more powerful in terms of discovering meaningful patterns hidden in the data-set. The nonlinear transformation is achieved by a mapping function $\Phi(\cdot)$ that maps the original space to feature space. Then KPCA can be achieved by performing classic PCA in nonlinear feature space. Alternatively, KPCA can be implemented by using the kernel function without explicitly exploring the form of mapping function (Schölkopf, Smola, and Müller 1998). The purpose of this approach is mainly to avoid the complexity of nonlinear mapping operation. In this article, we adopt the logarithmic function as the mapping function to take into consideration the multiplicative nature of SAR speckle noise. And we employ the mapping function instead of the kernel function, considering that the mapping function here is not complex and does not increase the dimensionality of the data.

3.2. KPCA local texture features

Texture features are usually predefined linear or nonlinear transformations of original image pixels. However, instead of using these predefined texture features, we design a set of totally data-driven local texture features based on the KPCA technique. These adaptive features are capable of revealing meaningful information hidden in image patches, while achieving Gaussian-like noise characteristics.

Assuming that the speckle noise is fully developed, a SAR image patch variable can be modelled as (Hoekman 2001):

$$\vec{\boldsymbol{y}} = (\vec{x}_1\vec{n}_1, \vec{x}_2\vec{n}_2, \ldots, \vec{x}_p\vec{n}_p)^{\mathrm{T}}, \tag{5}$$

where $\vec{x}_i$ and $\vec{n}_i$ are, respectively, the terrain backscatter intensity and the speckle intensity of the ith pixel in image patch. For fully developed speckle noise, $\vec{x}_i$ and $\vec{n}_i$ are independent and $\vec{n}_i$ is spatially uncorrelated. Accordingly, we denote the SAR image as a collection of all the image patches and by a data matrix:

$$\vec{\mathbf{Y}} = [\vec{\boldsymbol{y}}_1, \vec{\boldsymbol{y}}_2, \ldots, \vec{\boldsymbol{y}}_N]^{\mathrm{T}}, \tag{6}$$

where $\vec{\boldsymbol{y}}_t (t \in N)$ represents the tth patch, which is obtained by placing a small square window at the tth pixel (Figure 1). Essentially, the proposed KPCA model seeks linear PCA directions in nonlinearly transformed feature space instead of the original space. The transformation can be achieved by a nonlinear mapping function $\Phi(\vec{\boldsymbol{y}})$. To account for the multiplicative nature of SAR speckle noise, in this article, we define:

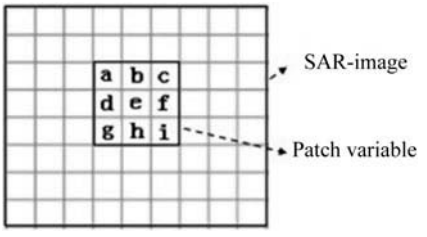

Figure 1. Illustration of patch acquisition in SAR sea ice image.

$$\Phi(\vec{\boldsymbol{y}}) = \log(\vec{\boldsymbol{y}}), \tag{7}$$

where $\log(\vec{\boldsymbol{y}})$ represents taking the logarithm of each element of $\vec{\boldsymbol{y}}$. Suppose $\Phi(\vec{\boldsymbol{y}})$ has been centralized, the covariance matrix in feature space is then

$$\mathbf{C} = 1/N \sum_{t=1}^{N} \Phi(\vec{\boldsymbol{y}}_t)\Phi^{\mathrm{T}}(\vec{\boldsymbol{y}}_t), \tag{8}$$

Note that $\mathbf{C}$ is a $p \times p$ matrix, because the mapping function $\Phi(\vec{\boldsymbol{y}})$ does not change the dimensionality of $\vec{\boldsymbol{y}}$. The KPCA can be achieved by performing singular value decomposition (SVD) on the covariance matrix in feature space:

$$\mathbf{C} = \begin{pmatrix} C_{aa} & C_{ab} & \ldots & C_{ai} \\ C_{ba} & C_{bb} & \ldots & C_{bi} \\ \vdots & \vdots & \ddots & \vdots \\ C_{ia} & C_{ib} & \ldots & C_{ii} \end{pmatrix} = \begin{pmatrix} \boldsymbol{w}_1^{\mathrm{T}} \\ \boldsymbol{w}_2^{\mathrm{T}} \\ \vdots \\ \boldsymbol{w}_p^{\mathrm{T}} \end{pmatrix}^{\mathrm{T}} \begin{pmatrix} \lambda_1 & 0 & \ldots & 0 \\ 0 & \lambda_2 & \ldots & 0 \\ \vdots & \vdots & \ddots & \vdots \\ 0 & 0 & 0 & \lambda_p \end{pmatrix} \begin{pmatrix} \boldsymbol{w}_1^{\mathrm{T}} \\ \boldsymbol{w}_2^{\mathrm{T}} \\ \vdots \\ \boldsymbol{w}_p^{\mathrm{T}} \end{pmatrix}, \tag{9}$$

where element C_{ab} of $\mathbf{C}$ represents the covariance between the two pixels at positions a and b in the image in feature space. So $\mathbf{C}$ provides a statistical description of the relationships between pixels in the SAR image. Pixels that do not belong to the same patch are considered uncorrelated. Hence, the size of the patch determines the scale of spatial patterns that can be described. Generally speaking, a bigger-sized patch considers longer-range correlations and hence is more capable of capturing larger-scale textural patterns in the SAR image. However, for SAR sea ice images, which do not have strong texture patterns, a small patch-size (e.g. 3×3) is sufficient.

The $p \times 1$ vectors $\{\boldsymbol{w}_j\}(j = 1, \ldots, p)$ denote mutually orthogonal PCA directions of sequentially largest variances in feature space. The KPCA texture features $\{\boldsymbol{z}_j\}(j = 1, \ldots, p)$ can be obtained by projecting the patches stack onto the PCA directions:

$$\boldsymbol{z}_j = \Phi\left(\vec{\mathbf{Y}}\right)\boldsymbol{w}_j (j = 1, \ldots, p). \tag{10}$$

The resulting variables $\{\boldsymbol{z}_j\}(j = 1, \ldots, p)$ are called principal components (PCs), whose variances are represented by $\{\lambda_i\}(i = 1, \ldots, p)$. As discussed in Section 3.1, while we adopt the mapping function for obtaining KPCA features, it is equivalent to follow the

approach presented in Schölkopf, Smola, and Müller (1998) by using the kernel function $k\left(\vec{\boldsymbol{y}}_t,\vec{\boldsymbol{y}}_q\right) = \log(\vec{\boldsymbol{y}}_t)\log\left(\vec{\boldsymbol{y}}_q^{\mathrm{T}}\right)$, where $\boldsymbol{y}_t$ and $\boldsymbol{y}_q$ represents two patch variables.

The above-described KPCA texture features assume several interesting characteristics that are of help in sea ice segmentation.

- The features admit Gaussian-like noise with stable variance. Although most statistical methods, e.g. PCA, *k*-means and GMM, require symmetrically distributed noise with a constant noise level, this requirement cannot be satisfied in the case of SAR imagery. Because of its multiplicative nature, the speckle noise renders the variance of $\vec{\boldsymbol{y}}$ unstable across the image, and the data distribution 'heavy-tailed'. Nevertheless, the KPCA features solve this problem by adopting a mapping function that maps the original domain into the logarithmic domain:

$$\boldsymbol{y} = \Phi(\vec{\boldsymbol{y}}) = \boldsymbol{x} + \boldsymbol{n}, \tag{11}$$

  where $\boldsymbol{x}$ and $\boldsymbol{n}$ are, respectively, the terrain backscatter intensity and speckle intensity in an image patch in the logarithmic domain. After being mapped nonlinearly into the logarithmic domain, the probability density function (PDF) of $\boldsymbol{n}$ is close to a Gaussian distribution, and the mean and variance of $\boldsymbol{n}$ do not change across the image (Hoekman 2001). Therefore, we can approximately treat $\boldsymbol{n}$ as Gaussian noise with zero mean and isotropic variance matrix, $\mathbf{I}_p\sigma^2$, where $\mathbf{I}_p$ denotes the $p \times p$ identity matrix. Not only does the distribution of $\boldsymbol{n}$ satisfy the assumptions implicit in the PCA model (Tipping and Bishop 1999), it also enables the resulting KPCA features to optimize the *k*-means algorithm, as proved in Section 3.2.
- The features are discriminative. The KPCA texture features are linear projections of image patches onto the leading principal axes. Since the principal axes reveal the largest variations in patch stack, the corresponding PCs therefore amount to linear texture patterns that reflect the greatest variations between different sea ice types. The subspace with the largest variance is very likely to be the subspace where sea ice classes demonstrate their differences. Suppose that texture patterns are similar within a certain class, but are different for different classes. Then the KPCA's goal of seeking subspaces with large variances will naturally drive it to find the subspaces that are capable of revealing between-class variations, instead of subspaces revealing within-class variations.
- The features are compact. In the KPCA domain, the signal is mainly captured by several leading PCs, while the last PCs are primarily due to noise. Therefore, dimension reduction can be achieved by preserving several leading PCs as texture features.
- The features are adaptive. For the Gabor filter and GLCM, it is always a hard task to select relevant texture features from all the available ones. However, it is not the case for the KPCA features, because they are totally data-driven and capable of automatically adapting to the 'best' transformations of the pixel values.
- Because of the orthogonal constraint, the KPCA features reflect mutually independent information and thus are capable of reducing information redundancy.

Therefore, the KPCA local texture features are powerful for sea ice segmentation. While in this article, we adopt KPCA features to feed the *k*-means algorithm, it is also promising

to combine them with other clustering or classification techniques for SAR sea ice monitoring.

3.3. The compatibility of KPCA texture features with the k-means algorithm

The KPCA technique is performed on the image patches to obtain a set of compact texture features. We then employ the *k*-means algorithm on the extracted KPCA texture features for sea ice segmentation. Hence, one essential issue is to ensure the compatibility of KPCA features with the *k*-means model. In the following, we prove that the *k*-means algorithm is a special case of the expectation maximization (EM) solution to Equation (4) and that KPCA features satisfy the assumptions of the *k*-means algorithm.

Following the typical formulation of the EM algorithm, we express Equation (4) as

$$\hat{\boldsymbol{l}} = \underset{l}{\operatorname{argmin}} \left\{ \sum_{t=1}^{N} R_t^i \left[\sum_{i=1}^{K} \ln p(l_t = i) + \ln|\boldsymbol{\Lambda}_i|^{-1/2} + 1/2 \left(\boldsymbol{y}_t^i - \boldsymbol{\mu}^i\right)^{\mathrm{T}} \boldsymbol{\Lambda}_i^{-1} \left(\boldsymbol{y}_t^i - \boldsymbol{\mu}^i\right) \right] \right\}. \tag{12}$$

As we can see, if $\boldsymbol{\Lambda}_i = \sigma^2 \mathbf{I}$ $(i = 1, 2, \ldots, K)$, classes are equally likely, and R_t^i is deterministic assignment, Equation (12) degrades to the object function of the *k*-means algorithm:

$$\hat{\boldsymbol{l}} = \underset{l}{\operatorname{argmin}} \left\{ \sum_{t=1}^{N} \sum_{i=1}^{K} \left(\boldsymbol{y}_t^i - \boldsymbol{\mu}^i\right)^{\mathrm{T}} \left(\boldsymbol{y}_t^i - \boldsymbol{\mu}^i\right)] \right\}. \tag{13}$$

Therefore, as it is a special case of the GMM, the *k*-means algorithm implicitly assumes that the noise follows an i.i.d. Gaussian distribution. Accordingly, to implement the *k*-means algorithm in our study, it is necessary to explore whether the noise in KPCA features satisfies the i.i.d. Gaussian distribution. We prove that this condition is, indeed, satisfied in the following.

In logarithmic feature space, following Equation (11), we express the centralized patch variable as

$$\boldsymbol{y} = \boldsymbol{x} + \boldsymbol{n}, \tag{14}$$

where $\mathbf{y} = [y_1, y_2, \cdots, y_p]^{\mathrm{T}}$, $\mathbf{x} = [x_1, x_2, \cdots, x_p]^{\mathrm{T}}$, and $\boldsymbol{n} = [n_1, n_2, \ldots, n_p]^{\mathrm{T}}$. Based on Equation (11), $\boldsymbol{n}$ roughly satisfies i.i.d. Gaussian distribution with variance matrix $\sigma^2 \mathbf{I}_p$. Since $\boldsymbol{x}$ and $\boldsymbol{n}$ are independent for fully developed speckle noise, we can get

$$\boldsymbol{\Sigma}_y = \boldsymbol{\Sigma}_x + \sigma^2 \mathbf{I}_p, \tag{15}$$

where $\boldsymbol{\Sigma}_y$ and $\boldsymbol{\Sigma}_x$ denote, respectively, the covariance matrices of $\boldsymbol{y}$ and $\boldsymbol{x}$. The PCA analysis can be achieved by performing SVD on $\boldsymbol{\Sigma}_x$.

$$\boldsymbol{\Sigma}_x = \mathbf{W}\mathbf{S}\mathbf{W}^{\mathrm{T}}, \tag{16}$$

where the matrix $\mathbf{W}$ is a matrix whose column vectors represent the PCA bases with sequentially largest variances, and $\mathbf{S} = \mathrm{diag}(s_1, \ldots, s_p)$ is a diagonal matrix with the diagonal elements being the variances of the PCs. Then, we have

$$\boldsymbol{\Sigma}_{\boldsymbol{y}} = \mathbf{W}\mathbf{S}\mathbf{W}^{\mathrm{T}} + \sigma^2\mathbf{W}\mathbf{W}^{\mathrm{T}} = \mathbf{W}\begin{bmatrix} s_1 + \sigma^2 & \cdots & 0 \\ \vdots & \ddots & \vdots \\ 0 & \cdots & s_p + \sigma^2 \end{bmatrix}\mathbf{W}^{\mathrm{T}}. \tag{17}$$

So we can see, $\boldsymbol{\Sigma}_{\boldsymbol{x}}$ and $\boldsymbol{\Sigma}_{\boldsymbol{y}}$ share the same PCA bases. As in Equation (10), the texture features can be obtained by projecting the image patch onto PCA bases:

$$\boldsymbol{z} = \mathbf{W}^{\mathrm{T}}\boldsymbol{y} = \mathbf{W}^{\mathrm{T}}\boldsymbol{x} + \mathbf{W}^{\mathrm{T}}\boldsymbol{n} = \boldsymbol{z}_{\boldsymbol{x}} + \boldsymbol{z}_{\boldsymbol{n}}, \tag{18}$$

where $\boldsymbol{z}_{\boldsymbol{x}} = \mathbf{W}^{\mathrm{T}}\boldsymbol{x}$ and $\boldsymbol{z}_{\boldsymbol{n}} = \mathbf{W}^{\mathrm{T}}\boldsymbol{n}$ stand, respectively, for the signal and noise parts in texture features $\boldsymbol{z}$. Denote the variance matrix of $\boldsymbol{z}$ by $\boldsymbol{\Sigma}_{\boldsymbol{z}}$:

$$\boldsymbol{\Sigma}_{\boldsymbol{z}} = \boldsymbol{\Sigma}_{\boldsymbol{z}_x} + \boldsymbol{\Sigma}_{\boldsymbol{z}_n} = \begin{bmatrix} s_1 & \cdots & 0 \\ \vdots & \ddots & \vdots \\ 0 & \cdots & s_p \end{bmatrix} + \begin{bmatrix} \sigma^2 & \cdots & 0 \\ \vdots & \ddots & \vdots \\ 0 & \cdots & \sigma^2 \end{bmatrix}. \tag{19}$$

Since $\boldsymbol{\Sigma}_{\boldsymbol{z}_n} = \sigma^2\mathbf{I}$, the assumption that the k-means algorithm makes about the noise distribution can be well satisfied. Although this property could not guarantee the convergence of the k-means algorithm to a global minimum, it provides theoretical assurance that the k-means performance can be optimized.

4. Sea ice segmentation based on KPCA texture features

In this section, we first introduce the data set adopted in this study. We then introduce the complete segmentation scheme. Each step in the segmentation scheme is illustrated and the tuning of parameters discussed.

4.1. Data set

An HH-polarization RADARSAT-2 image comprising several sea ice types located off the coast of Newfoundland, a Canadian island province, was provided by the CIS for this study. The image was acquired in ScanSAR Wide beam mode at 22:29:36 UTC on 16 March 2009. Given the large size (7291 pixels × 7296 pixels) of the original image scene (see Figure 2), a subset of 684 pixels × 544 pixels was used for fast processing (see Figure 4).

To evaluate segmentation results, it is important to know accurately the location and extent of different sea ice types. The CIS website provides daily regional ice charts, which provide a series of egg codes, indicating the sea ice concentrations, stages of development, and form of the ice for each segment of sea ice-covered regions. Figure 3 shows the daily regional ice-chart covering the study area. By carefully interpreting the egg codes for each segment of the study area, we found two sea ice types in Figure 4, i.e. the grey ice with a thickness of 10–15 cm and medium thick first-year ice with a thickness of 70–120 cm. Nevertheless, the ice-chart could not provide accurate spatial

Figure 2. RADARSAT-2 image (7291 pixels × 7296 pixels) covering the sea area nearby the Island of Newfoundland in Canada, ScanSAR Wide beam mode, HH polarization, taken at 22:29:36 on 16 March 2009.

information concerning sea ice distribution on the specific date that the image was acquired. Therefore, prior knowledge regarding the physical properties of different sea ice types should be utilized for interpreting the SAR sea ice image shown in Figure 3. Sea ice backscatter in SAR imagery depends primarily on the surface roughness and the dielectric constant of sea ice or open seawater (Carsey 1992). Generally speaking, a rougher surface enables more radiation to be backscattered to the sensor, causing brighter appearance in SAR imagery. The dielectric constant of sea ice decreases as the degree of salinity decreases. Lower dielectric constant generally causes stronger backscatter. This implies that thicker sea ice tends to assume brighter colour due to its lower salinity, and new or fresh sea ice appears darker in the image because of the relatively higher dielectric constant. Based on the above prior knowledge, we identify three main classes in Figure 4. First, because of higher backscatter return, the area marked with the circle indicates relatively thicker ice, possibly being medium-thick first-year ice with a thickness of 70–120 cm. Second, the diamond area indicates fresh/thin ice, possibly being grey ice with a thickness of 10–15 cm, considering the observed lower backscatter return. Third, the dark areas marked by the rectangle probably correspond to seawater, because seawater is assumed to have high salinity and also a smooth surface (under relatively calm conditions), and therefore tends to reflect most of radiation away from the SAR sensor by specular reflection when the wind speed is low. The above interpretation helps us to obtain labels for all the pixels in Figure 4, which enables us to evaluate the performance of the different algorithms under consideration.

4.2. Complete segmentation algorithm

By using KPCA and the *k*-means algorithm as building blocks, a coherent scheme for SAR sea ice segmentation can be assembled. Since the proposed segmentation scheme is primarily based on a KPCA local texture feature model, we refer to it as KPCA. Based on Equations (18) and (19), it is feasible to combine the KPCA texture features with other advanced statistical techniques, e.g. MRF and GMM. Nevertheless, our adoption of the

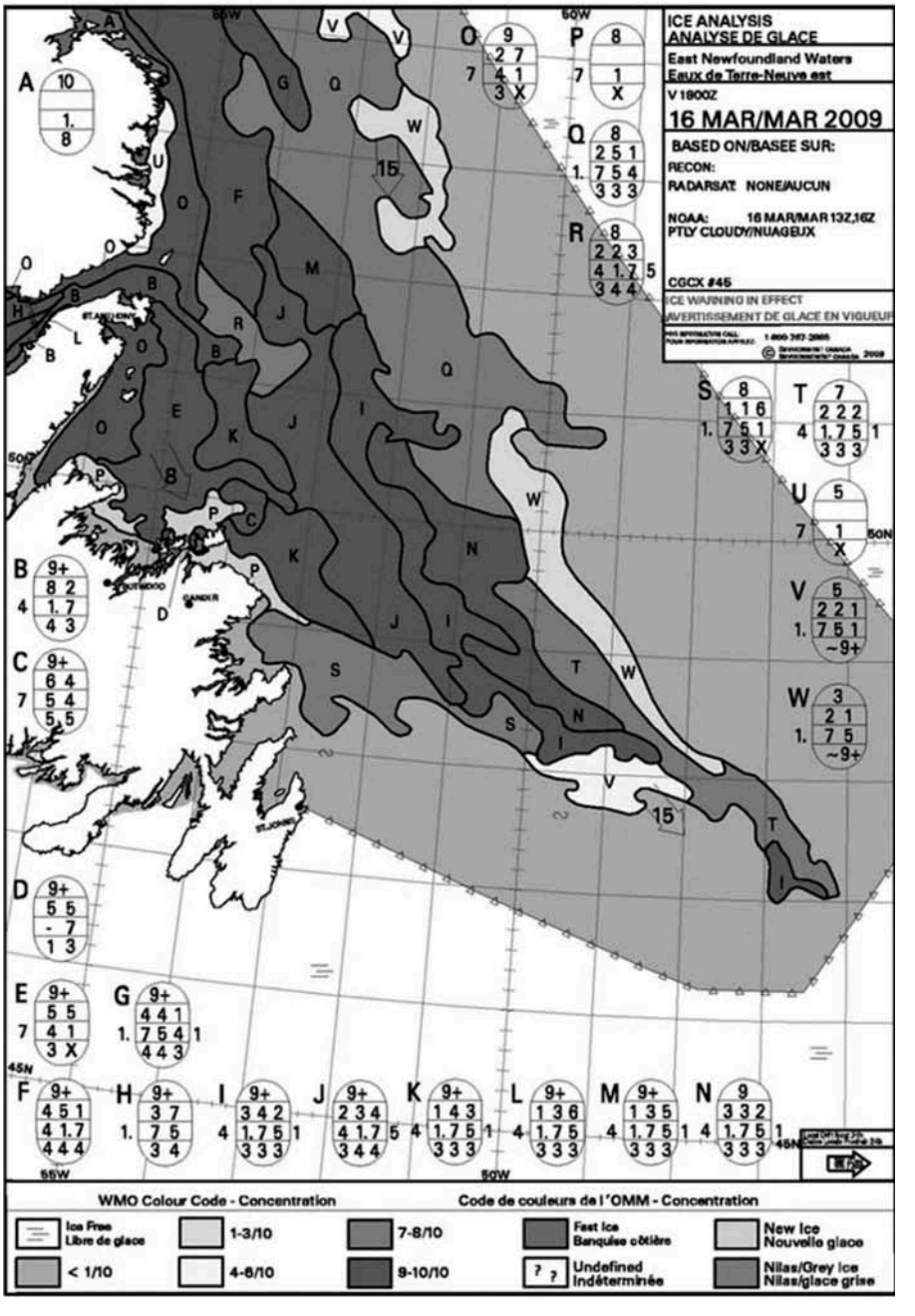

Figure 3. Daily regional ice-chart (for 16 March 2009) covering the study area.
Note: In this figure, the egg codes, i.e. the oval symbols, contain ice information of different regions, i.e. concentrations, stages of development (age), and form (floe size) of ice.

k-means algorithm is mainly based on considerations of its simplicity and speed. Figure 5 shows the flow chart of the proposed segmentation scheme. We discuss the detailed implementation of each step in the following.

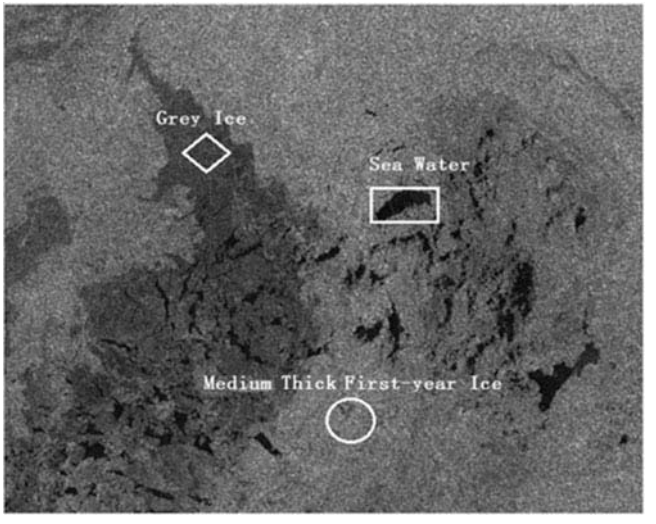

Figure 4. Subset taken from the sea ice region (684 pixels × 544 pixels).

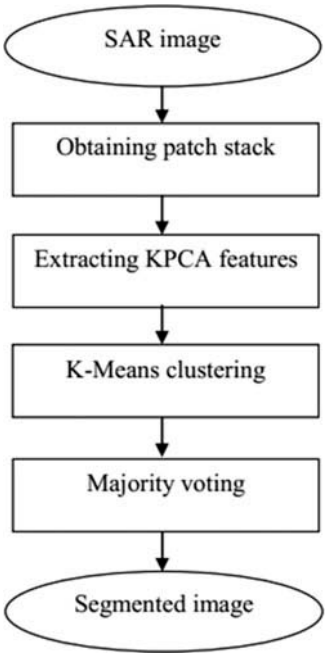

Figure 5. The flowchart of the proposed segmentation scheme.

4.2.1. *Obtaining patch stack*

The patch stack in Equation (6) is produced by extracting an image patch for each pixel in the image. One important issue is to determine the patch size. As discussed in Section 3.2, large-sized patches are more capable of capturing large-scale spatial patterns. However, large patches tend to erase detailed information at boundary areas. Since sea ice in SAR

images is generally devoid of strong texture patterns, we suggest that a small patch size (e.g. 3×3) is sufficient.

4.2.2. Extracting KPCA texture features

Given a patch stack, we extract KPCA texture features by using Equations (7)–(10). Since the first few PCs account for most of the data variance and the last few PCs are mainly due to noise, we want to adopt the first C PCs from Equation (10) that correspond to scene signals as features extracted. We employ the popular approach whereby C is determined by setting a threshold that corresponds to the first few C PCs explaining a particular percentage of the variation. We therefore select the first C PCs that account for 80% of the total variance.

4.2.3. k-Means clustering

Based on the KPCA features, we implement the k-means algorithm to segment the sea ice image. The determination of the number of modalities existing in the data set is still an open issue. While it can be treated as a model selection problem and solved by optimizing a certain criterion, searching for the best solution requires a lot of computation. For SAR sea ice image segmentation, we can obtain some prior information from the sea ice chart. The egg codes indicate the number of sea ice types present in a particular region. So in this article, we assume that the number of classes is already known.

k-Means clustering is very sensitive to initial parameter values. Poor assignment of initial parameters will produce a long convergence time. Good assignment, on the other hand, not only reduces computation time, but also increases the opportunity to approach the global optimum. Considering that the first PC provides a contiguous membership indicator for k-means (Ding and He 2004), we sort the first PC and then split the sorted PC values evenly into K groups. We use the mean values of the K groups as estimates of the initial class centres.

4.2.4. Outlier compensation via neighbourhood-based majority voting scheme

Although KPCA features are capable of resisting speckle noise, a certain amount of misclassification still happens because of inhomogeneous phenomena, e.g. ridges and rims (Shokr 1991). To further eliminate the artefacts from the segmentation results, we refine the labels produced by the k-means algorithm by removing such outlier anomalies. Since the artefacts are very small in size, the labels of the artefacts are different from the labels of the background. Accordingly, we can remove artefacts by forcing their labels to be the same as the majority labels in a local neighbourhood. In other words, the label of a pixel t is determined by the majority voting of its neighbouring pixels, $g\ \{g|g \in N(t)\}$.

$$l_t = \underset{g \in \mathrm{N}(t)}{\mathrm{mode}}\left(l_g\right). \tag{20}$$

The size of the neighbourhood $N(t)$ should be determined according to the size of the artefacts to be removed. In this article, we denote the size of neighbourhood by M. According to our experiments, $M = 49$ (7×7) achieved very good results.

5. Results and discussion

In this section, the results achieved by the proposed method are reported and discussed in comparison with several other popular methods. Before reporting the results on real SAR images, we first examine the results on simulated SAR sea ice images, where clean images with ice-like grey tones were degraded by speckle noise. In simulated study, the clean images were used as ground truth to produce numerical measures for performance evaluation. For real SAR images, the evaluation of segmentation result was by visual interpretation based on prior knowledge and ice-chart concerning sea ice types and their spatial distributions.

5.1. Results on simulated images

One clean image (Figure 6(*a*)) was degraded by speckle noise that satisfied a square root Gamma distribution (Xie, Pierce, and Ulaby 2002). Simulated images with different noise levels measured by equivalent number of looks (ENL) were used to feed segmentation methods in order to examine their robustness to varying noise levels.

On simulated sea ice images, we compared the proposed method with three popular methods, i.e. Gamma mixture (Samadani 1995), GLCM (Clausi and Yue 2004) and an MRF-based technique (Deng and Clausi 2005). For the MRF-based method, we adopted the grey tone values as features, used 150 EM iterations and 10,000 simulated-annealing iterations. For GLCM, we used 12 features (i.e. entropy, dissimilarity and correlation in four directions), 64 quantization levels, and a patch size of 15 pixels $\times$ 15 pixels.

Figure 6 provides the segmentation results achieved by different algorithms when ENL = 4. It suggests that the proposed method outperformed the other three techniques. As we can see, the Gamma mixture approach produced intense artefacts, because of the sensitivity of single pixels to speckle noise. The GLCM and MRF methods, although better at resisting the influence of speckle noise, produced certain misclassifications. For

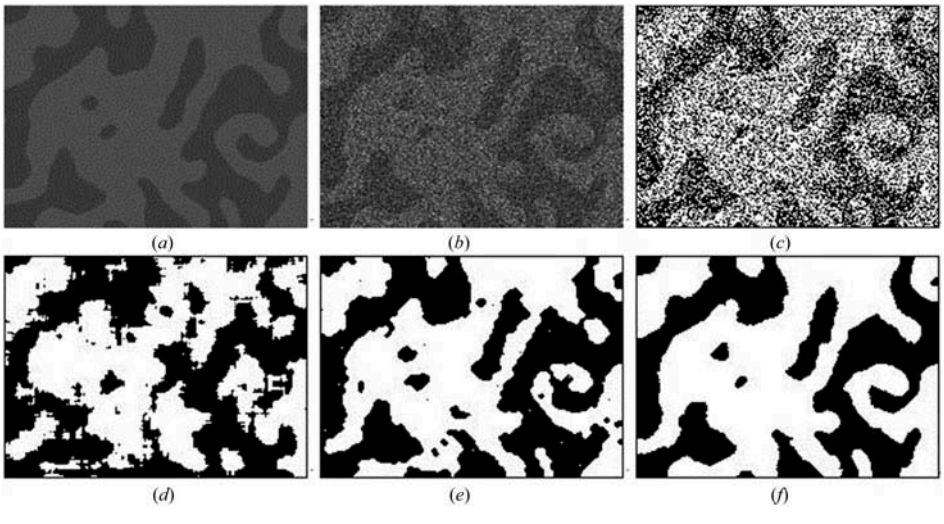

Figure 6. Simulated image segmented by different techniques, (*a*) true image, (*b*) image with speckle noise (L = 4), and images segmented by (*c*) Gamma mixture, (*d*) GLCM, (*e*) MRF, and (*f*) KPCA.

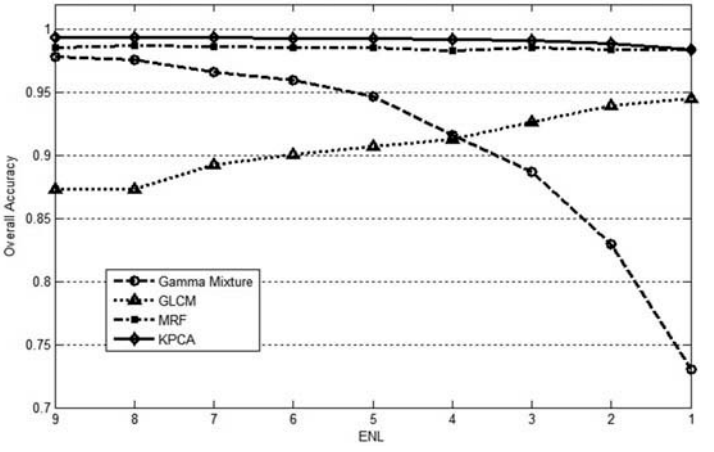

Figure 7. Plot of OA as a function of noise level as measured by the ENL.

example, GLCM failed to delineate the boundaries accurately; MRF also failed to provide smooth boundaries. KPCA nevertheless produced segmentation results that were very similar to the true image.

We adopt the overall accuracy (OA) measure for quantitative evaluation of the results. The OA is calculated as the ratio of the number of pixels that are correctly classified to the total number of pixels. Figure 7 shows the OA of different algorithms as a function of noise level measured by ENL. As we can see, the values of OA for the KPCA are higher than for all the other methods. As the noise level increases, the performance of the Gamma mixture method deteriorates sharply, while the MRF produces relatively stable results. It is remarkable that the OA of the GLCM increased slightly with the increase in noise level. This is probably because the performance of GLCM relies on strong textural patterns, which tend to be present when speckle noise is abundant. In contrast, KPCA produced stable OA values for a range of different noise levels, indicating that KPCA is not sensitive to speckle noise.

5.2. *Results using RADARSAT-2 SAR images*

We first ran the KPCA on a large image of 684 pixels $\times$ 544 pixels (Figure 4) to test the speed and accuracy. The results are shown in Figures 8 and 9. We then tested KPCA on three sub-images of the image shown in Figure 4 to compare with other algorithms. In this experiment, we replaced the Gamma mixture method with the *k*-means method (Redmund, Long, and Drinkwater 1998), and used the same parameter values as in the simulated study. Moreover, we implemented a so-called log *k*-means algorithm that transforms SAR images into the logarithmic domain before performing *k*-means clustering. The results are shown in Figures 10–12, and the summary of image information is shown in Table 1.

The results for the real SAR images are consistent with the results of the simulation. We can extract the following conclusions based on the results. First, KPCA can effectively resist the influence of speckle noise, while at the same time discriminate between different sea ice types very accurately. For example, Figure 9 suggests that KPCA can precisely delineate sea ice boundaries. Moreover, although it is challenging to identify small

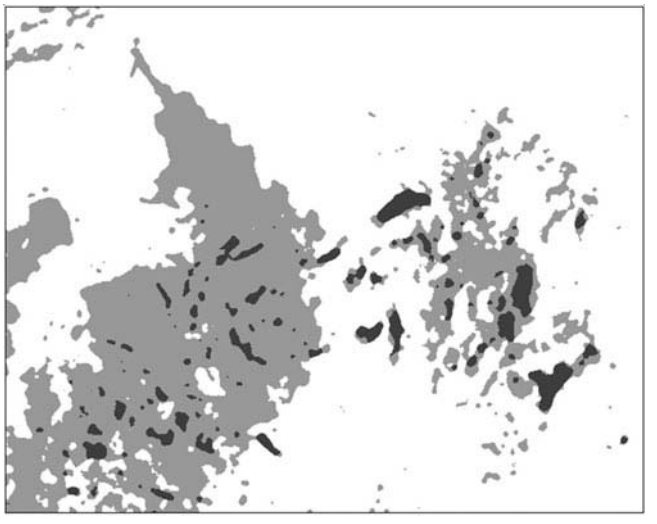

Figure 8. RADARSAT-2 images (684 pixels × 544 pixels) with three sea ice types segmented using the proposed KPCA algorithm. Under the MATLAB platform, it took 1.77 s to process this image on a PC with an Intel® 2.40 GHZ Quad-Core processor.

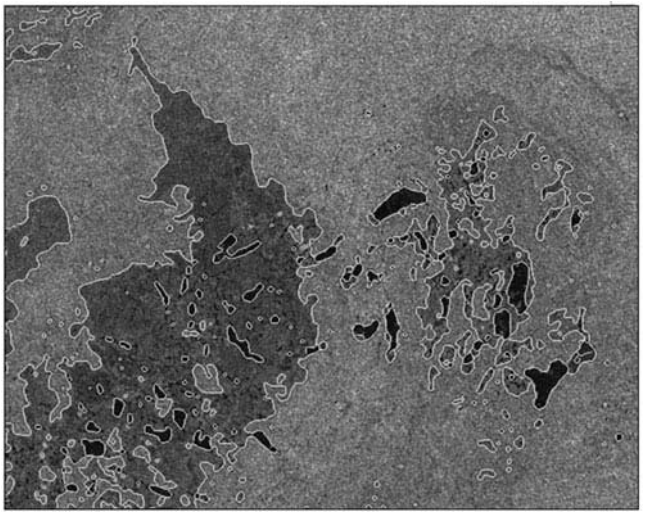

Figure 9. The KPCA segmentation results overlaid on the original SAR image (Figure 9).

classes, i.e. seawater in Figure 11 and 12, KPCA delineated seawater areas accurately. Another powerful model, MRF, although performing quite well, as shown in Figure 11, confused seawater with some grey ice, as shown in Figure 12.

Second, compared with GLCM, KPCA is more effective at discriminating different sea ice types and delineating ice boundaries. For example, in Figure 10, where GLCM misclassified the sharp boundary areas, KPCA, however, accurately delineated these boundaries. Moreover, in Figures 11 and 12, where GLCM failed to discriminate different

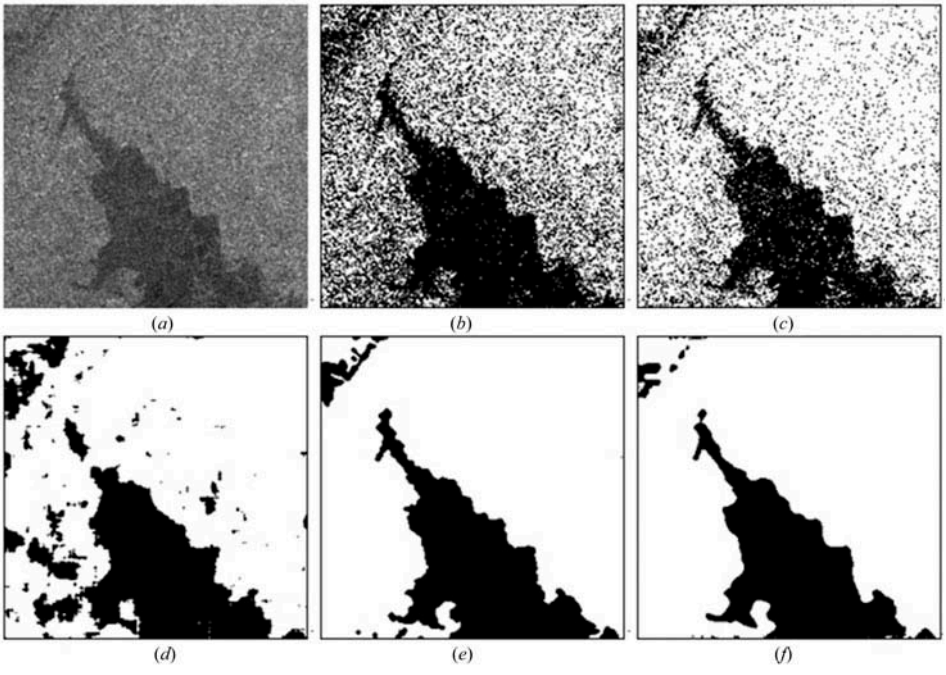

Figure 10. RADARSAT-2 images with two sea ice types labelled using each of the segmentation techniques. (*a*) Original image and images labelled using (*b*) *k*-means (*c*) log *k*-means, (*d*) GLCM, (*e*) MRF, and (*f*) KPCA techniques.

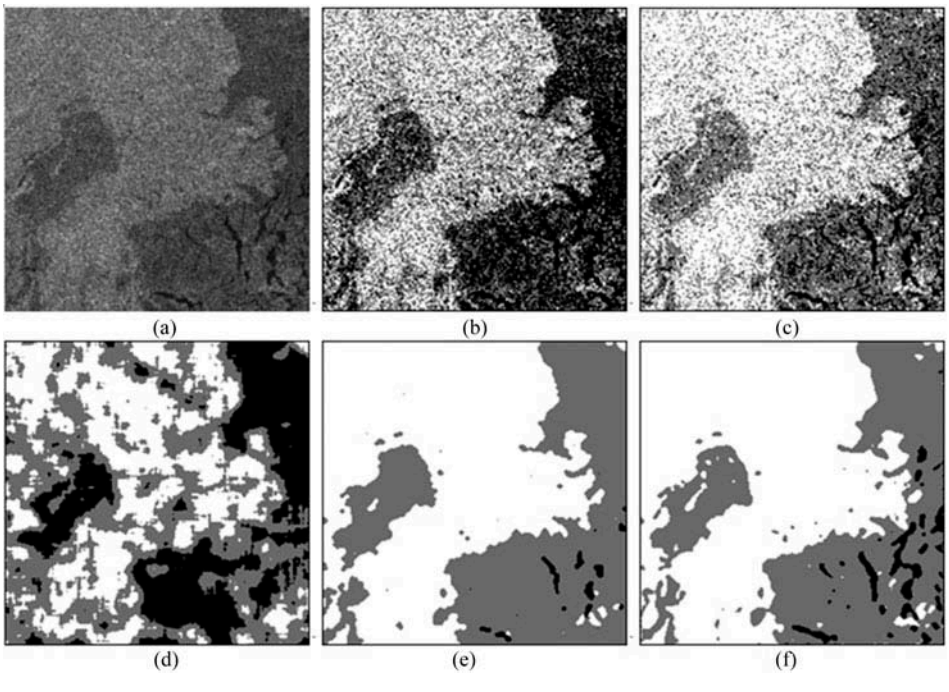

Figure 11. RADARSAT-2 images with three sea ice types labelled using each of the segmentation techniques. (*a*) Original image and images labelled using (*b*) *k*-means (*c*) log *k*-means, (*d*) GLCM, (*e*) MRF, and (*f*) KPCA techniques.

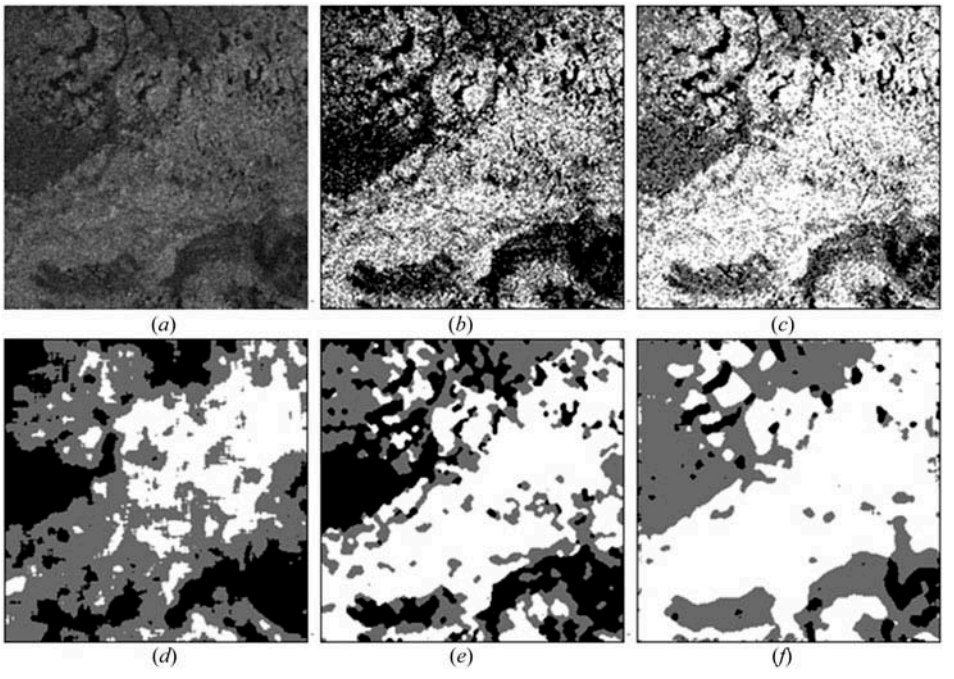

Figure 12. RADARSAT-2 images with three sea ice types labelled using each of the segmentation techniques. (*a*) Original image and images labelled using (*b*) *k*-means (*c*) log *k*-means and (*d*) GLCM, (*e*) MRF, and (*f*) KPCA techniques.

ice types, KPCA identified them accurately. We attribute the better performances of KPCA over GLCM to the following facts. (i) GLCM produces predefined texture features, which means that GLCM features are obtained in a prescribed manner. Accordingly, it is not able to adjust the transformation based on the characteristics of the current data set. On the other hand, KPCA is innately adaptive, where the coefficients of PCs are determined in a data-driven manner. KPCA is therefore more capable of discriminating between different sea ice types by adjusting its transformation to the textural characteristics of the current data set. To illustrate this, Figure 13 shows the histograms of the first KPCA component. It suggests that the first PC is already capable of revealing the modalities that were once hidden in the within-class variation. (ii) Unlike GLCM features whose statistical properties are complex and unpredictable, the KPCA features assume i.i.d. symmetric noise, which is more compatible with classical statistical clustering models, such as *k*-means. (iii) In contrast to GLCM, which relies on very large image patches, e.g. 15 pixels × 15 pixels, KPCA performs very well based on small-sized patches, e.g. 3 pixels × 3 pixels, thus is more capable of preserving sea ice boundaries.

Table 1. Summary of tested images.

Test site	Size (pixels)	Number of sea ice types
Figures 8 and 9	684 × 544	3 (Grey sea ice, Medium first-year sea-ice & sea water)
Figure 10	256 × 256	2 (Grey sea ice, Medium first-year sea-ice)
Figure 11	256 × 256	3 (Grey sea ice, Medium first-year sea-ice & sea water)
Figure 12	256 × 256	3 (Grey sea ice, Medium first-year sea-ice & sea water)

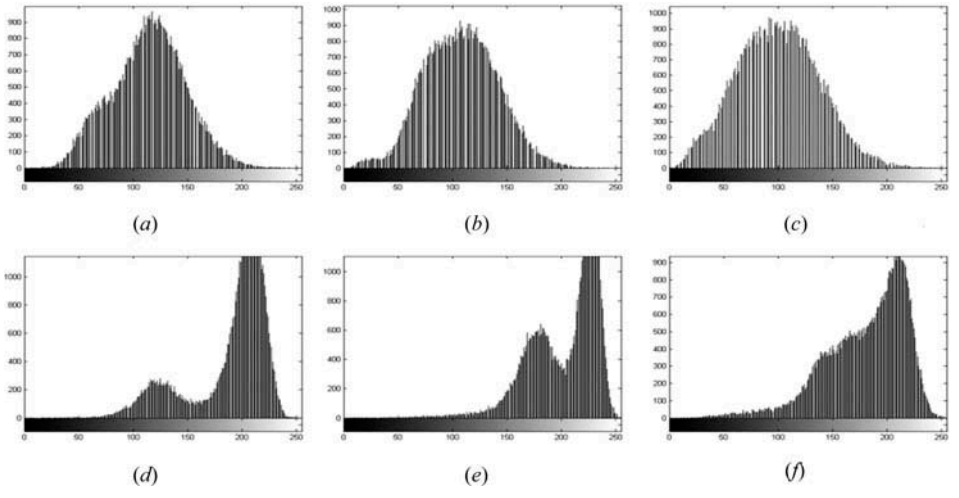

Figure 13. (*a*)–(*c*) are the histograms of three test images shown as Figures 10(*a*), 11(*a*), and 12(*a*), and (*d*)–(*f*) are the corresponding histograms for the first KPCA component.

Third, logarithmic projection should be adopted as a pre-processing step for SAR sea ice image segmentation in general. Most statistical methods, e.g. PCA, *k*-means, and GMM, rely on symmetrically distributed noise with a constant noise level. However, this requirement cannot be satisfied in the case of SAR imagery, where the multiplicative speckle noise assumes a 'heavy-tailed' distribution with unstable variance. Nevertheless, after mapping nonlinearly into the logarithmic domain, the PDF of the speckle noise is close to having a Gaussian distribution, with a constant mean and variance (Hoekman 2001). This conclusion is confirmed by experiments. For example, in Figures 10–12, where the classical *k*-means method confused seawater with grey ice, the log *k*-means method, which works in the logarithmic domain, demonstrated better separation of different sea ice types.

Last, KPCA is much more computationally efficient than other advanced algorithms, such as GLCM and MRF. All the algorithms were implemented in MATLAB and ran on a PC with an Intel® 2.40 GHZ Quad-Core processor. It is impressive that KPCA took only 1.77 s to process a large image (i.e. Figure 4) that consisted of 684 pixels × 544 pixels. Moreover, to process a 256 pixel × 256 pixel sub-image, it took *k*-means, KPCA, GLCM and MRF 0.038 s, 0.199 s, 113.090 s, and 5049.462 s, respectively.

6. Conclusions

In this article, we have presented a KPCA local texture feature model for fast and accurate SAR sea ice image segmentation. We performed KPCA on the image patches to extract compact and discriminative texture features with Gaussian-like noise characteristics. These KPCA texture features are totally data-driven and capable of revealing between-class variations. Moreover, since the noise in KPCA features follows an i.i.d. Gaussian distribution, KPCA features are comparable with the *k*-means algorithm. The combined use of KPCA features and the *k*-means algorithm constitutes a coherent and powerful scheme for SAR sea ice segmentation. To remove the artefacts from the segmented image, we proposed to refine the results of *k*-means using a neighbourhood-based majority voting

scheme. We compared our segmentation scheme with several other popular methods (i.e. *k*-means, Gamma mixture, GLCM, and MRF) using both simulated SAR images and RADARSAT-2 sea ice images. The results were evaluated by both visual interpretation and quantitative measures and suggested that KPCA achieved higher accuracy than the other techniques referred to. Moreover, KPCA achieved very high time-efficiency, thus may better support the operational segmentation of sea ice.

Acknowledgements

The authors thank the Canada Ice Service (CIS) for providing RADARSAT-2 data for research purposes and the anonymous reviewers for their valuable comments.

References

Baraldi, A., and F. Parmiggiani. 1995. "An Investigation of the Textural Characteristics Associated with Gray Level Co-Occurrence Matrix Statistical Parameters." *IEEE Transactions on Geoscience and Remote Sensing* 33 (2): 293–304. doi:10.1109/36.377929.

Barber, D. G., and E. F. Ledrew. 1991. "SAR Sea Ice Discrimination Using Texture Statistics: A Multivariate Approach." *Photogrammetric Engineering & Remote Sensing* 57 (4): 385–395.

Burns, B. A., E. S. Kasischke, and D. R. Nuesch, 1982. "Extraction of Texture Information from SAR Data: Application to Ice and Geological Mapping." International Symposium on Remote Sensing of Environment, Fort Worth, TX, December 6–10, 861–868.

Carsey, F., ed. 1992. *Microwave Remote Sensing of Sea Ice*, Vol. 68, 462 p. Geophysical Monograph Series. Washington, DC: AGU.

Clausi, D., and B. Yue. 2004. "Comparing Cooccurrence Probabilities and Markov Random Fields for Texture Analysis of SAR Sea Ice Imagery." *IEEE Transactions on Geoscience and Remote Sensing* 42 (1): 215–228. doi:10.1109/TGRS.2003.817218.

Clausi, D. A. 2001. "Comparison and Fusion of Co-Occurrence, Gabor and MRF Texture Features for Classification of SAR Sea-Ice Imagery." *Atmosphere-Ocean* 39 (3): 183–194. doi:10.1080/07055900.2001.9649675.

Clausi, D. A. 2002. "An Analysis of Cooccurrence Texture Statistics as a Function of Grey Level Quantization." *Canadian Journal of Remote Sensing* 28 (1): 45–62. doi:10.5589/m02-004.

Deng, D., and D. A. Clausi. 2005. "Unsupervised Segmentation of Synthetic Aperture Radar Sea Ice Imagery Using a Novel Markov Random Field Model." *IEEE Transactions on Geoscience and Remote Sensing* 43 (3): 528–538. doi:10.1109/TGRS.2004.839589.

Ding, C., and X. He, 2004. "K-Means Clustering via Principal Component Analysis." In *Proceeding of International Conference on Machine Learning (ICML 2004)*, July, 225–232. Banff: ACM.

Frost, V. S., J. A. Stiles, K. S. Shanmugan, and J. C. Holtzman. 1982. "A Model for Radar Images and Its Application to Adaptive Digital Filtering of Multiplicative Noise." *IEEE Transactions on Pattern Analysis and Machine Intelligence* PAMI-4 (2): 157–166. doi:10.1109/TPAMI.1982.4767223.

Haralick, R. M., K. Shanmugam, and I. Dinstein. 1973. "Textural Features for Image Classification." *IEEE Transactions on Systems, Man and Cybernetics* 3 (6): 610–621. doi:10.1109/TSMC.1973.4309314.

Havercamp, D., L. Soh, and C. Tsatsoulis. 1993. "A Dynamic Local Thresholding Technique for Sea Ice Classification." *Proceeding of IGARSS* 2: 638–640.

Heolbaek-Hansen, E., H. Thjelmeland, O. Johannessen, M. T. Olaussen, and R. Karpuz. 1989. "Speckle Reduction and Maximum Likelihood Classification of SAR Images from Sea Ice Recorded during MIZEX 87." *Proceeding of IGARSS* 2: 755–758.

Hoekman, D. H. 2001. "Speckle Ensemble Statistics of Logarithmically Scaled Data". *IEEE Transactions on Geoscience and Remote Sensing* 29: 180–182.

Karvonen, J. 2004. "Baltic Sea Ice SAR Segmentation and Classification Using Modified Pulse-Coupled Neural Networks." *IEEE Transactions on Geoscience and Remote Sensing* 42 (7): 1566–1574. doi:10.1109/TGRS.2004.828179.

Kuan, D. T., A. A. Sawchuk, T. C. Strand, and P. Chavel. 1985. "Adaptive Noise Smoothing filter for Images with Signal-Dependent Noise." *IEEE Transactions on Pattern Analysis and Machine Intelligence* PAMI-7 (2): 165–177. doi:10.1109/TPAMI.1985.4767641.

Lee, J. S. 1980. "Digital Image Enhancement and Noise filtering by Use of Local Statistics." *IEEE Transactions on Pattern Analysis and Machine Intelligence* PAMI-2 (2): 165–168. doi:10.1109/TPAMI.1980.4766994.

Ochilov, S., and D. Clausi. 2012. "Operational SAR Sea Ice Image Classification." *IEEE Transactions on Geoscience and Remote Sensing* 50: 4397–4408. doi:10.1109/TGRS.2012.2192278.

Redmund, Q., D. Long, and M. Drinkwater. 1998. "Polar Sea Ice Classification Using Enhanced Resolution NSCAT Data." *Proceeding of IGARSS* 4: 1976–1978.

Rivas, M., and A. Stoffelen. 2011. "New Bayesian Algorithm for Sea Ice Detection with Quikscat." *IEEE Transactions on Geoscience and Remote Sensing* 49: 1894–1901. doi:10.1109/TGRS.2010.2101608.

Samadani, R. 1995. "A Finite Mixtures Algorithm for Finding Proportions in SAR Images." *IEEE Transactions on Image Processing* 4 (8): 1182–1186. doi:10.1109/83.403427.

Schölkopf, B., A. Smola, and K. R. Müller. 1998. "Nonlinear Component Analysis as a Kernel Eigenvalue Problem." *Neural Computation* 10: 1299–1319. doi:10.1162/089976698300017467.

Shokr, M. E. 1991. "Evaluation of Second-Order Texture Parameters for Sea Ice Classification from Radar Images." *Journal of Geophysical Research* 96 (C6): 10625–10640. doi:10.1029/91JC00693.

Shuchman, R. A., C. C. Wackerman, A. L. Maffett, R. G. Onstott, and L. L. Sutherland 1989. "The Discrimination of Sea Ice Types Using SAR Backscatter Statistics." Proceeding of IGARSS, Vancouver, BC, July 10–14, 381–385.

Soh, L. K., and C. Tsatsoulis. 1999. "Texture Analysis of SAR Sea Ice Imagery Using Gray Level Cooccurrence Matrices." *IEEE Transactions on Geoscience and Remote Sensing* 37 (2): 780–795. doi:10.1109/36.752194.

Swan, A., and D. G. Long. 2012. "Multiyear Arctic Sea Ice Classification Using Quikscat." *IEEE Transactions on Geoscience and Remote Sensing* 50: 3317–3326. doi:10.1109/TGRS.2012.2184123.

Tipping, M. E., and C. M. Bishop. 1999. "Mixtures of Probabilistic Principal Component Analyzers." *Neural Computation* 11 (2): 443–482. doi:10.1162/089976699300016728.

Xie, H., L. Pierce, and F. Ulaby, 2002. "Despeckling SAR Images Using a Low Complexity Wavelet Denoising Process." *Proceeding of IGARSS* 1: 321–324.